Emerging Hydrogenated Semiconductors

Emerging Hydrogenated Semiconductors:

Synthesis, Properties and Applications

By

Xiaodan Wang,
Beibei Wang
and Hao Shen

**Cambridge
Scholars**
Publishing

Emerging Hydrogenated Semiconductors:
Synthesis, Properties and Applications

By Xiaodan Wang, Beibei Wang and Hao Shen

This book first published 2024

Cambridge Scholars Publishing

Lady Stephenson Library, Newcastle upon Tyne, NE6 2PA, UK

British Library Cataloguing in Publication Data
A catalogue record for this book is available from the British Library

ISBN: 978-1-0364-1281-4
ISBN (Ebook): 978-1-0364-1282-1

CONTENTS

LIST OF TABLES AND ILLUSTRATIONS vii

PREFACE xvi

CHAPTER 1 INTRODUCTION 1
- 1.1. What are the emerging hydrogenated semiconductor materials?
- 1.2. Why are the hydrogenated semiconductor materials so important?
- 1.3. The hydrogenated semiconductor materials: state of the art

CHAPTER 2 FABRICATION METHODS 9
- 2.1. The main synthesis methods in the classification
- 2.2. Comparing their pros and cons, the technical bottleneck of conventional methods and some promising methods

CHAPTER 3 DENSITY FUNCTIONAL THEORY 20
- 3.1. Introduction
- 3.2. Mechanism of H_2 hydrogenation
- 3.3. Mechanism of H hydrogenation
- 3.4. Mechanism of H^+ hydrogenation

CHAPTER 4 BASIC PHYSICAL PROPERTIES 40
- 4.1. Explain why hydrogen doping can improve physical properties of semiconductor materials from a physical point of view
- 4.2. Taking $HNdNiO_3$ as an example, the interrelationship between surface engineering, structure, physical properties and final performance is systematically revealed

CHAPTER 5 HYDROGENATED MATERIALS FOR ENERGY APPLICATIONS 48
- 5.1. Introduction
- 5.2. $H\text{-}TiO_2$ as a photoanode for photoelectrochemical hydrogen production
- 5.3. $H\text{-}Li_4Ti_5O_{12}$ as an electrode of lithium ion batteries
- 5.4. $HSrCoO_{2.5}$ as a solid electrolyte in hydrogen fuel cells
- 5.5. $H\text{-}Cs_2AgBiBr_6$ as an electrode for perovskite solar cells

CHAPTER 6 HYDROGENATED MATERIALS FOR NANOELECTRONICS 75
6.1. Introduction
6.2. H-Graphene for field effect transistors
6.3. H-$NdNiO_3$ for memory resistor
6.4. H-doped α-Fe_2O_3 for spin-based computing devices

CHAPTER 7 HYDROGENATED MATERIALS FOR SENSING APPLICATIONS 86
7.1. Introduction
7.2. H-TiO_2 Nanosheets for volatile organic compound (VOC) vapours detection
7.3. Hydrogenated graphene for NO_2 gas sensor
7.4. Hydrogenated CeO_2 nanofibers for acetone gas detection
7.5. Hydrogenated ZnO nanoparticles for ethanol gas detection

CHAPTER 8 HYDROGENATED MATERIALS FOR BIOLOGICAL APPLICATIONS 105
8.1. Introduction
8.2. Hydrogenated TiO_2 for cancer photothermal therapy
8.3. Fe@γ-Fe_2O_3@H-TiO_2 nanocomposites for imaging-guided photothermal cancer therapy

CHAPTER 9 OUTLOOK 118

REFERENCES 121

APPENDIX A 137

INDEX 138

LIST OF TABLES AND ILLUSTRATIONS

Table 2-1. Comparison of low-temperature H and room-temperature H^+ hydrogenation with traditional hydrogenation methods.

Table 5-1. The charge transfer behaviours of H-TiO_2 samples treated T_{wire} = 1600, 1700 and 1800°C and its impact on the PEC activity.

Table 5-2. Summary of hydrogenation-property experiments.

Fig. 1-1. Atomic structure of the of (a) crystalline and (b) amorphous hydrogenated amorphous silicon.

Fig. 1-2. Structure of (a) graphene and (b) hydrogenated graphene.

Fig. 1-3. (a) Core-shell crystal structure and narrowing band gap model. (b) Hydrogenation of white pristine TiO_2 to black TiO_2. (c) and (d) High-resolution transmission electron microscope (TEM) images of pristine TiO_2 and black TiO_2, respectively, confirming the core-shell structure of black TiO_2 by comparison.

Fig. 1-4. The interrelationship between the superior properties of hydrogenated semiconductors and their wide range of applications.

Fig. 2-1. Photos of P25 treated under H_2 for 0-20 days at 35 bar H_2 and room temperature.

Fig. 2-2. Digital pictures of pristine TiO_2 and H-TiO_2 nanowires annealed in hydrogen at various temperatures (300-550°C).

Fig. 2-3. (a) Absorption spectra and (b) photos of pristine TiO_2 and black TiO_2.

Fig. 2-4. Strategies for the hydrogenation of Pt promoted pristine TiO_2 to black TiO_2.

Fig. 2-5. Scheme of the facile hydrogenation of TiO_2 in the presence of Pd, in which ambient H_2/Ar (10%) gas flow is introduced.

Fig. 2-6. Scheme of black TiO_2 nanotubes by electrochemical reduction and the corresponding colour changes.

Fig. 2-7. Scheme of black TiO_2 prepared by high-energy proton implantation.

Fig. 2-8. Work principle of ionic liquid gating and the corresponding colour changes.

Fig. 2-9. Experimental set-up of low-temperature H hydrogenation.

Fig. 2-10. (a) Experimental set-up of room temperature H^+ hydrogenation. (b) The role of a circular electromagnetic coil in the H^+ hydrogenation process.

Fig. 3-1. Atomic structure of the stoichiometric rutile $TiO_2(110)$ surface. Oxygen atoms are shown in red, Ti atoms in grey. The two- and threefold-coordinated O sites and the fivefold-coordinated Ti sites are labelled by O_{2c}, O_{3c} and Ti_{5c}, respectively.

Fig. 3-2. Hydrogenation pathways of molecular hydrogen in contact with the $TiO_2(110)$ rutile surface with an initial hydrogen coverage of 0 ML with corresponding energy barriers E_B.

Fig. 3-3. (a)-(c) Atomistic structures of $TiO_2(110)$ with 1/4, 1 and 9/8 ML surface coverages. (d) Gibbs free energy of the different surface coverages vs. hydrogen chemical potential and partial pressure of atomic hydrogen at T=265°C. (e) Hydrogenation pathways of atomic hydrogen in contact with the (110) rutile surface with an initial hydrogen coverage of 1 ML with corresponding energy barriers E_B.

Fig. 3-4. (a) Adsorption free energy change for H incorporation in TiO_2 lattice as a function of temperature and pressure. (b) Like (a) but with molecular hydrogen as reference. (c) DFT cohesive energy with respect to atomic hydrogen. (d) Percentage of broken Ti-O bonds as a function of N and H concentration in wt.%. (e) Mean Ti-O bond lengths as a function of N and H concentration in wt.%. (f)-(h) Examples of relaxed TiO_2 model slabs with compositions $Ti_{48}O_{96}H_{12+N}$, N = 0, 36, 72.

Fig. 3-5. (a) Top view of the $TiO_2(110)$ rutile surface. (b) Side view of the employed slab supercell consisting of 4 Ti-O layers representing the $TiO_2(110)$ surface. (c) Penetration ratio of vertically impinging H radicals as a function of initial kinetic energy.

Fig. 3-6. The lateral positions of H radicals with initial kinetic energy of 0.1, 1, 3, 5, 10, 20, 40 and 80 eV that penetrated the rutile slab.

Fig. 3-7. (a-f) Typical trajectory of an H radical impinging the TiO_2 surface with a kinetic energy of 0.1, 1, 10, 20, 40 and 80 eV, respectively. (g) Penetration depth of vertically impinging H radicals as a function of initial kinetic energy.

Fig. 4-1. Scheme of hydrogenated materials with modulated electronic structures for nanoelectronics, energy and catalytic applications.

Fig. 4-2. Summary and technical roadmap of hydrogenated materials.

Fig. 4-3. (a) Coupling among ion, charge and lattice, via ionic intercalation can induce the lattice expansion and the charge doping. (b) Scheme of ionic liquid gating. (c) Phase transformation between NNO and the new phase H-NNO with giant lattice expansion. (d) Depth profiles of H ions for SIMs measurement of NNO and H-NNO.

Fig. 4-4. (a) Temperature-dependent electrical resistivity and metal-insulator transition with hydrogen-ion intercalation. (b) Optical transmittance of the pristine NNO and hydrogenated H-NNO. (c,d) Soft X-ray absorption spectra of the Ni L-edge and O K-edge of the pristine and hydrogen-intercalated H-NNO phase. (e,f) Energy band structure variation before and after hydrogen intercalation, in which the doped electron occupies the empty Ni–O hybrid orbital, where Δ represents the charge-transfer energy from O2p to Ni3d.

Fig. 4-5. Fabrication details of the micropattern with selective area phase transformation in the ionic liquid gating process for the (a) side and (b) top views, respectively.

Fig. 4-6. (a) Microscopic profile pattern of the origin NNO and H-NNO. (b) Electric conductivity variation with hydrogen intercalation. (c) Profile of the lattice expansion in (a). (d) Conductive profile corresponding to the surface profile in (c). (e) I–V curves of the pristine and gated areas in (b). (f) Electric-field-controlled hydrogen-intercalation-induced micropattern “IOP CAS”.

Fig. 5-1. (a) Measured photocurrent density for $H\text{-}TiO_2$ nanowires at 1.23 V_{RHE} as a function of H_2 annealing temperature. (b) J-V curves collected from pristine TiO_2 and $H\text{-}TiO_2$.

Fig. 5-2. (a) IPCE and (b) M-S plots of pristine TiO_2 and H-TiO_2.

Fig. 5-3. TEM, HR-TEM images and FFT patterns of (a-c) pristine TiO_2 and (d-f) H-TiO_2 nanorods treated at T_{wire}=1700°C. (g-h) The corresponding [O]/[Ti] ratios obtained from the quantification of the acquired EELS spectra.

Fig. 5-4. (a) Optical absorption and (b) Tauc plots of optical absorption curves for pristine TiO_2 and H-TiO_2 nanorods treated at T_{wire}=1600, 1700 and 1800°C, respectively.

Fig. 5-5. (a) J-V curves of pristine TiO_2 and H-TiO_2 nanorods in 1 M KOH solution in the dark and under solar illumination. (b) Mott-Schottky plots of pristine TiO_2 and H-TiO_2 nanorods treated at T_{wire}=1600, 1700 and 1800°C, respectively.

Fig. 5-6. (a) O1s and (b) Ti2p XPS spectra of pristine and H-TiO_2 samples treated at T_{wire}=1600, 1700 and 1800°C, respectively. (c) Localized densities of states (LDOS) in arbitrary units along the surface normal for a surface hydroxylated rutile (110) surface slab (left) and a slab model with additional hydrogen atoms in the subsurface region (right).

Fig. 5-7. TEM, HR-TEM and FFT images of H-TiO_2 at (a-c) 5 and (d-f) 40 mins treatment time, respectively. [O]/[Ti] composition ratios of the (g) pristine TiO_2 and H-TiO_2 at (h) 5 and (i) 40 mins treatment time, respectively.

Fig. 5-8. (a) Optical absorption spectra and (b) Tauc plot of pristine TiO_2 and H-TiO_2 at different treatment time.

Fig. 5-9. (a) J-V curves of pristine TiO_2 and H-TiO_2 at different treatment times in 1 M KOH solution in the dark and under solar illumination. (b) M-S plots of pristine TiO_2 and H-TiO_2 at different treatment times.

Fig. 5-10. Scheme for the fabrication of H-LTO NWAs.

Fig. 5-11. (a,b) Cross-sectional SEM and (c,d) TEM images of H-LTO NWAs annealing at 600°C. (e) Ti 2p core level XPS spectra of H-LTO NWAs and LTO NWAs, together with the difference in their spectra.

Fig. 5-12. The discharge curves of (a) H-LTO NWAs and (b) LTO NWAs. (c) Specific discharge capacities at various C rates. (d) Cycling performances at the rate of 5 C. (e) Cyclic voltammograms. (f) Nyquist plots.

Fig. 5-13. Optical absorption spectra of the SCO and H-SCO phases.

Fig. 5-14. (a) Temperature-dependent Nyquist plots of the impedance spectra for H-SCO measured at the atmosphere of forming gas (H_2:Ar = 10:90). (b) Comparison of proton conductivity in H-SCO with other solid oxide ionic conductors. (c) Top and (d) side view of the hydrogen diffusion within H-SCO crystalline structures. Arrows named as 'I' and 'II' represent two subsequent steps during the diffusion.

Fig. 5-15. (a) Environmental atmosphere dependence of the OCV for a dual-chamber SOFC. (b) Temperature-dependent OCV for a planar dual-chamber fuel cell.

Fig. 5-16. (a) UV-vis and (b) PL spectra of the $Cs_2AgBiBr_6$ perovskite films with different hydrogenation time. (c) The formation energies of H_1(in), H_2(in) and H_3(in). (d) Schematic band coupling models of H_n(in) (n = 1, 2, 3) showing energy level positions when the H 1s orbital is coupled to anion (forming donor) and cation (forming acceptor) levels. (e) Bader charge variations of Ag, Bi and Cs atoms in the host and next to the interstitial H* in the H_n(in) polyhedrons.

Fig. 5-17. (a) Current density-voltage (J-V) curve of the $Cs_2AgBiBr_6$ PSCs with different hydrogenation time (0, 600 and 1200 s). Inset: schematic of the layered perovskite solar cell. (b) J-V curves under reverse and forward bias of 1200 s hydrogenated $Cs_2AgBiBr_6$.

Fig. 6-1. (a) The Raman changes of H-Gr with an increase in hydrogen coverage at 300 K. (b) I_D/I_G and $I_D/I_{D'}$ as a function of hydrogen coverage. (c) Raman mapping of I_D/I_G for H-Gr at hydrogen coverage of 25%. Scale bar 5 mm. (d) The recovery of Raman spectra of H-Gr treated by ex-situ heating.

Fig. 6-2. (a,b) The evolution of optical absorption spectra of graphene and H-Gr and their estimated band gaps as a function of hydrogen coverage. (c,d) The full recovery of the optical absorption spectra and band gaps of H-Gr (25%) to the pristine graphene state after thermal treatment at 550 K under Ar atmosphere as a function of annealing time.

Fig. 6-3. (a) Scheme of H-Gr's FETs. (b) I–V source-drain characteristics as the gate bias was increased from -40 to +20 V. (c) Change in current on the sweep of a back-gate voltage.

Fig. 6-4. Scheme of device fabrication process for asymmetrical proton concentration.

Fig. 6-5. X-ray absorption spectroscopy (XAS) of pristine NNO and H-NNO.

Fig. 6-6. Two-terminal current-voltage (IV) characteristics of the devices with differently processed Pt electrodes.

Fig. 6-7. IV characteristics of the asymmetrical device (H-Pt/NNO/NH-Pt) with gradually increasing the sweeping width of voltages.

Fig. 6-8. Secondary ion mass spectroscopy (SIMs) depth profiles of hydrogen (H), oxygen (O), aluminium (Al) and nickel (Ni) in our protonic memory resistors at the vertical direction of (a) NH-Pt electrode and (b) H-Pt electrode.

Fig. 6-9. ERDA measurements of α-Fe_2O_3 samples that are (a) undoped, and either (b) H-annealed or (c) Ar-annealed at 250°C.

Fig. 6-10. RRBS measurements of α-Fe_2O_3 samples (a) H-annealed and (b) Ar-annealed at 250°C.

Fig. 6-11. (a) Scheme of α-Fe_2O_3 crystal unit cell and the spin alignment at $T < T_M$ (left) and $T > T_M$ (right). (b) M(T) curve of undoped α-Fe_2O_3 during up/down temperature sweeps. (c) Unit cell of H-doped α-Fe_2O_3 with in-plane L orientation throughout the temperature range, deduced from the transition-less M(T) curve (d). (e) Unit cell of H-doped α-Fe_2O_3 after restoration step in 100% O_2 atmosphere, exhibited the out-of-plane to in-plane L transition, inferred from the return of the Morin transition in M(T) (f).

Fig. 7-1. (a) XRD pattern, (b) SEM, (c) TEM and (d) HRTEM images of the as-prepared TiO_2 nanosheets.

Fig. 7-2. (a) XRD patterns of the samples hydrogenated at different temperatures for 24 h. (b) SEM image of the sample hydrogenated at 600°C.

Fig. 7-3. On/off sensing curves of the sensors based on the as-prepared TiO_2 nanosheets and the hydrogenated samples to different concentrations of (a) ethanol, (b) acetone, (c) triethylamine and (d) formaldehyde at 350°C.

Fig. 7-4. Response curves of the sensors based on the as-prepared TiO_2 nanosheets and the hydrogenated samples toward different concentrations of (a) ethanol, (b) acetone, (c) triethylamine and (d) formaldehyde at 350°C.

Fig. 7-5. XPS spectra of the four types of TiO_2 nanosheets: (a) the overview spectra, (b) Ti2p XPS spectra and (c-f) O1s XPS spectra of TiO_2, TiO_2-H-400, TiO_2-H-500 and TiO_2-H-600, respectively.

Fig. 7-6. (a) Atomic structure of the anatase TiO_2 (001) surface. (b,c) Scheme of the hydrogenation reaction of TiO_2 nanosheets with exposed {001} facets. (d-f) Sensing reaction mechanism on the anatase TiO_2 (001) surface.

Fig. 7-7. Raman spectra of (a) unpatterned pristine graphene and (b) PGS before and after exposure to NO_2 gas.

Fig. 7-8. Raman spectra obtained from the HGS after treatment with hydrogen plasma for different times.

Fig. 7-9. (a) On/off response of the PGS and HGS measured at NO_2 concentrations of 0.4, 0.6, 1, 2, 4, 8, 12 and 20 ppm. (b) $\Delta G/G_0$ versus I_D/I_G for various graphene-based sensors.

Fig. 7-10. SEM images of (a) CeO_2-P, (b) CeO_2-H-180, (c) CeO_2-H-480, (d) CeO_2-H-680 samples. The CeO_2-H-680 sample: (e) TEM image, (f) HR-TEM image, (g) EDS spectra: Ce (orange) and O (green).

Fig. 7-11. (a) Overview XPS, (b-e) Ce3d and (f-i) O1s XPS spectra of all samples.

Fig. 7-12. (a) Ce^{3+} ion and (b) oxygen vacancy percentage versus hydrogen annealing temperature.

Fig. 7-13. (a) Response of the pristine and hydrogenated CeO_2 sensor to 100 ppm acetone at different operating temperatures, (b) Response to the acetone concentrations of 5-2000 ppm.

Fig. 7-14. Gas sensing mechanism of pristine CeO_2 and hydrogenated CeO_2 towards acetone gas.

Fig. 7-15. (a) SEM image and (b) XRD pattern of the pristine ZnO nanoparticles.

Fig. 7-16. (a–c) SEM images and (d) XRD patterns of the ZnO nanoparticles hydrogenated at 500°C for 12, 24 and 36 h.

Fig. 7-17. (a) Response and recovery curves of the four types of sensors based on the pristine and hydrogenated ZnO nanoparticles towards different concentrations of ethanol at 350°C. (b) The plots of the response of the four types of sensors based on the pristine and hydrogenated ZnO nanoparticles versus the test gas concentration for ethanol at 350°C.

Fig. 7-18. (a) overview, (b) Zn 2p and (c–f) O 1s spectra XPS spectra of pristine and hydrogenated ZnO nanoparticles.

Fig. 7-19. (a) Structural model of wurtzite ZnO. (b) Scheme of hydrogenation reaction of ZnO nanoparticles.

Fig. 7-20. Scheme of sensing reaction occurring at the surface of ZnO nanoparticles at atomic level.

Fig. 8-1. TEM of (a) H-TiO$_2$ and (b) H-TiO$_2$-PEG.

Fig. 8-2. UV–vis–NIR absorption spectra of the pristine and H-TiO$_2$ NPs.

Fig. 8-3. Temperature evaluation of H-TiO$_2$-PEG NPs and pure water with 808 nm laser irradiation for different times.

Fig. 8-4. Viability of (a) MCF-7 and (b) 4T1 cells treated with or without H-TiO$_2$-PEG NPs and 808 nm laser irradiation at 2 W cm^{-2} for 5 mins.

Fig. 8-5. (a) Photothermal images of tumour site in Laser group and Laser + NPs group during 5 mins irradiation of 2 W cm^{-2} NIR. (b) Whole body temperature images of the mice at the 5th mins of NIR irradiation. (c) Temperature change (ΔT) of tumour sites during NIR irradiation. (d) The relative tumour volume of the mice after different treatments.

Fig. 8-6. SEM and inset TEM images of (a) TiO$_2$ and (b) H-TiO$_2$, respectively. The scale bars of inset images are 50 nm.

Fig. 8-7. (a) SEM and (b) TEM images of α-Fe$_2$O$_3$.

Fig. 8-8. (a) TEM and (b) HAADF-STEM and EDS line scanning, and (c) HRTEM image of Fe@γ-Fe$_2$O$_3$@H-TiO$_2$. (d) Room temperature Mössbauer spectra of Fe@γ-Fe$_2$O$_3$@H-TiO$_2$.

Fig. 8-9. (a) DRS spectra and (b) optical band gaps of TiO_2 and H-TiO_2, respectively. (c) Magnetization curve of Fe@γ-Fe_2O_3@H-TiO_2.

Fig. 8-10. (a) Photothermal activity of TiO_2, H-TiO_2 and Fe@γ-Fe_2O_3@H-TiO_2 NCs. (b) Photothermal conversion characterizations of Fe@γ-Fe_2O_3@H-TiO_2 aqueous solution with various concentrations.

Fig. 8-11. The electron loops between H-TiO_2 and γ-Fe_2O_3.

Fig. 8-12. HeLa cells viability after incubation with Fe@γ-Fe_2O_3@H-TiO_2 NCs in (a) dark and (b) with 1.5 W cm^{-2} 808 nm laser irradiation for 5 mins.

Fig. 8-13. In vivo (a) MR imaging, (b) PT imaging, and (c) PA imaging of Fe@γ-Fe_2O_3@H-TiO_2 NCs with intravenous injection and magnetic-targeted delivery.

Fig. 9-1. Technical roadmap of hydrogenated semiconductors for variety of applications.

PREFACE

Hydrogenated semiconductors are gaining worldwide attention for their unique properties and applications, but there is a lack of comprehensive books or reviews on the subject. It is crucial to gather and explain the latest developments in this emerging field.

For more than 10 years, we have focused on improving hydrogenation technologies for creating black titanium dioxide. Our innovative methods have achieved the highest reported photocurrent density for black TiO_2 towards solar water splitting, overcoming challenges of traditional processes like high temperature and prolonged treatment time.

This book focuses on the recent advancements in hydrogenated semiconductors and their diverse applications in transistors, gas sensors, solar water splitting, solar cells, fuel cells and photothermal tumour therapy. We elucidate the correlation between surface modification, structures, properties and functions, providing a microscopic explanation for their exceptional properties. The book not only suggests future directions toward further progress in hydrogenation technology and hydrogenated semiconductors, but also introduces several promising hydrogenation techniques which vigorously promote the progress from basic research to practical application, enabling the efficient transformation from scientific research results to industrialization.

This book introduces emerging materials to a wide audience and serves as a valuable reference for scientific researchers working on new materials and devices.

We would like to thank L. Mayrhofer, M. Keunecke, M. Hoefer, S. Estrade, L. Lopez-Conesa, M. Moseler, F. Peiró, L. Schaefer, X. Meng and J. Chu for the long-term collaboration. We express our gratitude to C. Ji for her contributions to editing and proofreading the book.

Xiaodan Wang
Beibei Wang
Hao Shen

April 2024

CHAPTER 1

INTRODUCTION

1.1. What are the emerging hydrogenated semiconductor materials?

First of all, let's consider: what is a hydrogenated semiconductor material? As the name suggests, it is a new semiconductor material obtained through hydrogen doping in the original semiconductor. This arises the question, what changes does it bring to the structures, properties and functions of this kind of semiconductor? Let's start with the important discovery of three hydrogenated semiconductors in the history of science.

1. Hydrogenated amorphous silicon

Hydrogenated amorphous silicon is the first artificial hydrogenated semiconductor material in the history of human science. Fig. 1-1 shows that this hydrogenated amorphous silicon has a completely different crystal structure to crystalline silicon, and it produces many dangling bonds due to the disordered state, forming Si-H chemical bonds with hydrogen atoms.

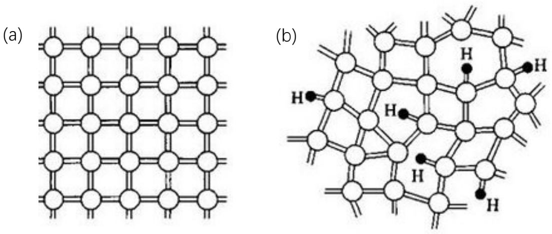

Fig. 1-1. Atomic structure of the of (a) crystalline and (b) amorphous hydrogenated amorphous silicon.

Since 1950, some pioneers have tried, without success, to prepare such materials by methods including evaporation and sputtering. After more than 20 years of effort, in 1975, the British scientist W. E. Spear successfully prepared this kind of material by the method of glow discharge,[1] and then in 1976, the American scientist D. E. Carlson prepared an amorphous silicon solar cell with a power conversion efficiency of 6%,[2] opening up a new type of hydrogenated amorphous silicon field, which has a wide range of applications in renewable energy applications, such as amorphous silicon solar cells.

2. Hydrogenated graphene

In 2009, British scientists Andre Geim and Kostya Novoselov published an article in *Science* pointing out that a new material called 'graphane' was successfully prepared through the mutual reaction of hydrogen and graphene.[3] Fig. 1-2 shows the crystal structure of graphane, which differs from graphene, forming a C-H bond on its two-dimensional surface. This new material is a derivative of graphene, and is of breakthrough significance because, by adjusting the amount of hydrogen doping, graphene can be changed from a semimetal to a semiconductor material with adjustable band gap, which will have a wide range of applications in the field of optoelectronic nanodevices and renewable energy.

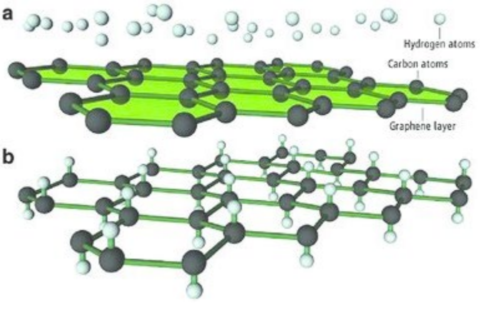

Fig. 1-2. Structure of (a) graphene and (b) hydrogenated graphene.

3. Hydrogenated titanium dioxide

In 2011, American scientists Xiaobo Chen and Samuel Mao reported in the journal *Science* that they innovatively prepared black titanium dioxide (H-TiO_2) under high-pressure hydrogen treatment.[4] Figure 1-3 shows the unique core-shell crystal structure of black TiO_2 and the energy diagram with a reduced band gap. It has been confirmed to have a wider band for absorbing light. In addition to visible light, it can also absorb ultraviolet and infrared light. Further, it has excellent photocatalytic characteristics. Since 2011, black TiO_2, which combines high sunlight absorption and ultra-high photocatalysis features, has become a cutting-edge material in academia and industry.

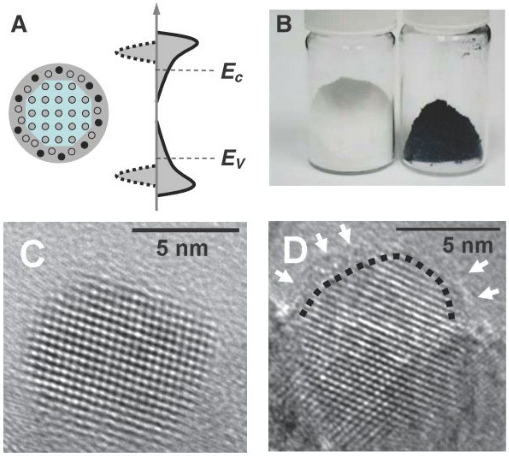

Fig. 1-3. (a) Core-shell crystal structure and narrowing band gap model. (b) Hydrogenation of white pristine TiO_2 to black TiO_2. (c) and (d) High-resolution transmission electron microscope (TEM) images of pristine TiO_2 and black TiO_2, respectively, confirming the core-shell structure of black TiO_2 by comparison.

1.2. Why are the hydrogenated semiconductor materials so important?

At that time, the doping of semiconductors was due to the need to modify the properties of intrinsic semiconductors, and their structural, electrical and optical properties could be changed through doping. In view of this idea, scientists have tried doping various elements, some of which have been relatively successful, but most of which have not, and the mechanism behind them remains unclear. American scientist Steven C. Erwin pointed out in *Nature* in 2005 that doping is limited by various factors. The semiconductor crystal structure and facet, for instance, have an important impact on the doping effect.[5]

Compared with the doping of other elements, hydrogen doping has the following advantages: because the diameter of hydrogen is the smallest of all elements, the tolerance of the semiconductor to hydrogen doping is the highest, and the hydrogen doping can reach the maximum concentration without destroying the crystal structure of the semiconductor matrix. However, due to the Coulomb interaction, the crystal structure will be distorted to reach charge equilibrium, resulting in new electronic band structures of the crystalline. At the subsurface, hydrogen and the semiconductor atoms form chemical bonds, which change the charge distribution of the original semiconductor materials, resulting in a charge redistribution, thereby fundamentally changing the properties of the materials such as optoelectronics, catalysis and photothermal, thus broadening the wide application of materials in various application fields.[6] Therefore, the surface engineering of hydrogen doping is like a magic wand, which has the great effect of turning stones into gold.

1.3. The hydrogenated semiconductor materials: state of the art

Because of the above three materials, which demonstrate excellent properties, wide applications and the beneficial features of hydrogen doping, a variety of hydrogenated semiconductor materials have sprung up. These have demonstrated novel structures, superior properties, outstanding functions and their wide and huge potential in various application fields.

1. Hydrogenated materials for energy applications

Photoelectrochemical hydrogen production: Since black titanium dioxide was reported in *Science* in 2011, this new material has attracted significant attention from scientists worldwide. In the same year, the American Yat Li's research group treated titanium dioxide nanowires with molecular hydrogen, and they found that, compared with the pristine TiO_2 nanowires, hydrogenated TiO_2 showed enhanced photocurrent density and efficient charge carrier separation and transport. This can be attributed to the increased donor density of TiO_2 through the creation of oxygen vacancies by hydrogenation, indicating the huge application potential in the field of photoelectrochemical hydrogen production.[7]

Lithium-ion batteries: In 2012, Chinese scientists Xiaogang Zhang and Guozhong Cao developed hydrogenated $Li_4Ti_5O_{12}$ nanowire arrays as an anode for high-rate lithium-ion batteries, overcoming the limitations of the original material's low conductivity and low-rate capabilities. They found that the nanowire arrays have a highly oriented one-dimensional structure and a multi-level porous composition that enable rapid Li^+ and electron diffusion, and that the hydrogenation process produces Ti^{3+} sites that further enhance the electron conductivity. The experimental results show that hydrogenated $Li_4Ti_5O_{12}$ exhibits high discharge capacity and voltage stability at different current rates, demonstrating its potential as a high-performance anode for lithium-ion batteries.[8]

Hydrogen fuel cells: In 2022, Chinese scientists Jian Wu and Pu Yu reported in the journal Nature Energy that a novel solid oxide proton conductor $HSrCoO_{2.5}$ exhibits high proton conductivity at low temperatures from 40 to 140°C. It experimentally reveals that the proton conductivity of $HSrCoO_{2.5}$ is attributed to the high proton concentration and well-ordered oxygen vacancy channels provided by the hydrogen-intercalated brownmillerite crystalline structure. It also demonstrates that the solid oxide material can be used as a proton conduction electrolyte in hydrogen fuel cells, greatly improving the conversion efficiency from chemical energy to electrical energy.[9]

Solar cells: In 2022, the Prof. Manling Sui's team in China adjusted the band gap of the $Cs_2AgBiBr_6$ film from 2.18 eV to 1.64 eV through hydrogenation, a process which also optimized the carrier mobility and carrier lifetime. This significantly improved the power conversion efficiency of the lead-free $Cs_2AgBiBr_6$ perovskite solar cell by 6.37%, overcoming the intrinsic limitations that the wide bandgap of $Cs_2AgBiBr_6$ leads to its poor light absorption capacity and low power conversion efficiency.[10]

2. Hydrogenated materials for nanoelectronics

Transistors: In 2012, the team of American Professor Jeffrey W. Baldwin discovered that the band gap can be induced by hydrogenated graphene, and the types of most charge carriers can be changed. They found that the band gap in hydrogenated graphene is temperature-dependent and increases along with hydrogen coverage. This work demonstrates the ability to control the most charge carriers and open the band gap in hydrogenated graphene, indicating the great potential for chemically modified graphene p-n junctions.[11]

Spin transistors: In 2013, Professor Sang Wook Han, a Korean scientist, reported the temperature dependence of mass magnetizations and magnetic hysteresis loops of hydrogenated MoS_2 samples. The hydrogenation of a single crystal MoS_2 at 300°C for 1 hour caused its out-of-plane easy axis, which exhibited ferromagnetic behaviour and showed the potential of hydrogenated MoS_2 in a new spintronic device.[12]

Non-volatile memory: In 2016, Professor Junwoo Son, a Korean scientist, prepared hydrogenated $NdNiO_3$ by atomic hydrogenation with noble metal, fabricated a metal-$NdNiO_3$-metal device structure with asymmetric proton concentration, and realized a resistively switched memory through ion transport of protons at the metal-hydrogenated $NdNiO_3$ interface. This is of great significance for the development of energy-saving switching devices for non-volatile memory and neuromorphic applications.[13]

3. Hydrogenated materials for sensing applications

Infrared sensors: In 2017, Canadian scientist Bright C. Iheanacho fabricated a novel lateral infrared photodetector using the three-dimensional structure of ZnO nanowire core and a-Si:H thin film shell, which showed a low dark current and high light on/off ratio under the irradiation of pulsed light with a wavelength of 1.55 μm. This can be used to develop large-area infrared image sensor arrays.[14]

Gas sensors: In 2023, Prof. Zhenxing Zhang's team in China used hydrogen annealing to enhance the gas sensing performance of cerium oxide (CeO_2) nanofibers in acetone gas detection. It was found that hydrogen annealing did not change the crystal structure or nanofiber morphology of CeO_2 compared with pure CeO_2, but increased the concentration of Ce^{3+} ions and oxygen vacancies. Gas sensing experiments, with the hydrogenated CeO_2 sensor on acetone, showed enhanced gas sensing performance such as good selectivity, repeatability and long-term stability, which are attributed to the increase in Ce^{3+} ion concentration and oxygen vacancies.[15]

4. Hydrogenated materials for biological applications

Photothermal tumour therapy: In 2022, Chinese scientists Yucai Wang and Jun Jiang turned the metal oxide material MoO_3 into H_xMoO_3 through a hydrogenation reaction treated with metal acid, which can effectively convert near-infrared (NIR) light energy into heat. It shows that under NIR light, H_xMoO_3 exhibits high photothermal conversion efficiency and achieves a high tumour suppression rate, opening the door to intelligent photothermal tumour therapy.[16]

Biosensors: In 2022, scientists from the Netherlands and China collaborated to analyse the structure and performance characteristics of the bowtie triangle ring composed of hydrogenated boron phosphide (BP), using density functional theory (DFT) and finite element method (FEM). The results show that hydrogenated BP has high carrier mobility for both electrons and holes, the transmission spectrum of the microstructure can be controlled by adjusting its carrier density, and the theoretical sensitivity of its microstructure is found to be sufficient to diagnose COVID-19, which may be a promising tool for rapid diagnosis of COVID-19.[17]

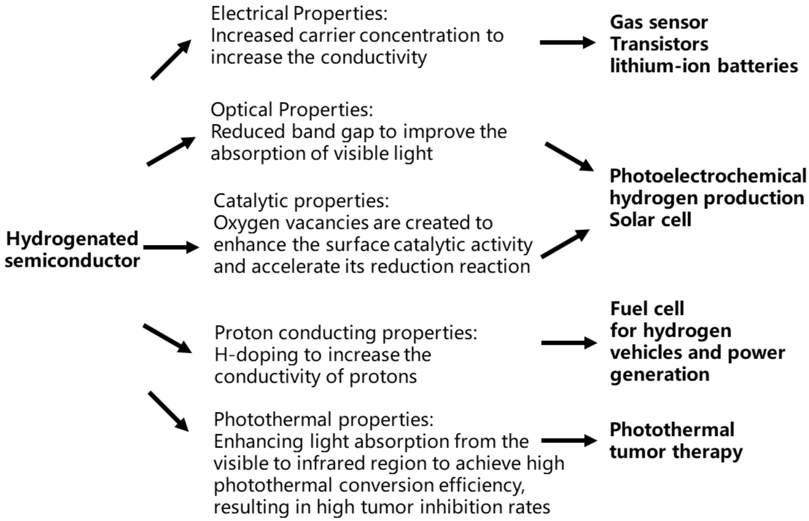

Fig. 1-4. The interrelationship between the superior properties of hydrogenated semiconductors and their wide range of applications.

According to the specific applications of hydrogenated semiconductor materials in different fields, we briefly summarize the interrelationship between hydrogenated semiconductors and their excellent properties, as well as wide applications (Fig. 1-4). This shows that there is plenty of room to develop the hydrogenated semiconductor materials, but many scientific and technological issues must be addressed in fundamental and applied research of this kind.

In this book, we will introduce and discuss several types of hydrogenated semiconductor materials in detail, reveal the effects of hydrogen doping on the interrelationship between the structure, physical properties and functions of these semiconductor materials, and explain the physical picture behind them. In addition, this book will mainly serve those engaged in basic research of materials science in universities and scientific research institutions, and engineers engaged in the research and development of new materials, principles and devices in enterprises, providing a new vision and dimension for their work.

CHAPTER 2

FABRICATION METHODS

Here we will introduce some typical and practical hydrogenation methods, which are presented in details in the review articles.[7,18-83]

2.1. The main synthesis methods in the classification

High-pressure H_2

Chen et al. reported in 2011 *Science* the breakthrough milestone: the first hydrogenation method-like high-pressure H_2 hydrogenation.[4] The specific hydrogenation details are as follows: The white TiO_2 powders underwent a vacuum treatment for 1 h upon placement in the sample chamber of a Hy-Energy PCTPro high-pressure hydrogen system, followed by hydrogenation in a 20 bar H_2 atmosphere at approximately 200°C for a duration of 5 days.

This method promotes the hydrogenation reaction by increasing the H_2 pressure to increase the flow rate of H_2 on the surface of the material while decreasing the temperature. Figure 1-3b in Chapter 1 shows that white TiO_2 turns into black TiO_2 after hydrogenation. They did not systematically change the hydrogenation parameters to hydrogenate TiO_2, the hydrogenation–property relation is unknown. Due to its high pressure and long processing time, it is not suitable for practical applications.

Lu et al. (2014) reported the hydrogenation of TiO_2 at room temperature by increasing the pressure of H_2 to 35 bar.[50] Here's how: The starting material utilized in this study was commercial P25 TiO_2 (Degussa) with an anatase/rutile ratio of 80/20. Initially, 0.5 g of P25 TiO_2 powders were subjected to a 24 h vacuum treatment, followed by hydrogenation at 35 bar H_2 and room temperature within a custom-made stainless-steel cell (500 mL). The resulting product colour P25 was obtained for 3-20 days. Figure 2-1 shows the colour change of TiO_2 at different treatment times. Although a safe and facile route is developed to prepare black titania at room temperature, harsh hydrogenation conditions prevent its practical application.

Fig. 2-1. Photos of P25 treated under H_2 for 0-20 days at 35 bar H_2 and room temperature.

High-temperature H_2

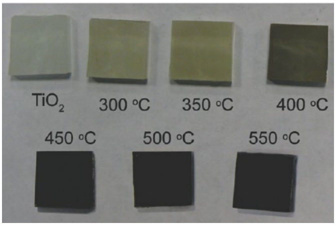

Fig. 2-2. Digital pictures of pristine TiO_2 and H-TiO_2 nanowires annealed in hydrogen at various temperatures (300-550°C).

Due to the harsh conditions of the high-pressure H_2 hydrogenation method, Wang et al. reported in 2011 *Nano Letters* that TiO_2 was hydrogenated using H_2 at one atmospheric pressure.[7] The details of their hydrogenation are as follows: The TiO_2 nanowire arrays were initially annealed in air at 550°C for 3 h, followed by a subsequent annealing process in H_2 atmosphere for 30 mins at temperatures ranging from 200 to 550°C. The annealing was carried out using a custom-built tube furnace filled with ultrahigh purity hydrogen gas supplied by Praxair. Figure 2-2 shows the colour change of TiO_2 at different hydrogenation temperatures. In this method, the hydrogenation of TiO_2 was promoted by increasing the hydrogenation temperature (400°C, 1h) while decreasing the hydrogen pressure (1 bar).

High-temperature H^+

Wang et al. reported a new hydrogenation method in 2013 Adv. Funct. Mater..[37] The hydrogenation details are as follows: The process of hydrogenating TiO_2 was conducted in a thermal plasma furnace using hydrogen plasma for a duration of 4 to 8 h at a temperature of 500°C, with a plasma input power of 200 W. Figure 2-3 shows the change in colour of TiO_2 before and after hydrogenation.

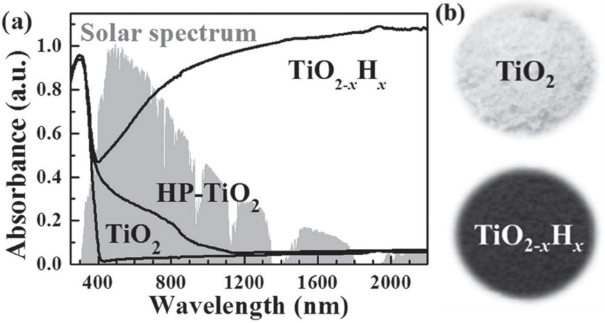

Fig. 2-3. (a) Absorption spectra and (b) photos of pristine TiO_2 and black TiO_2.

However, the hydrogenation methods described above still require harsh conditions with high pressure, high temperatures and prolonged treatment times.

Noble metal-assisted H

In order to solve these problems, Zhu et al. reported in 2014 *Chemical communications* the noble metal-assisted H hydrogenation method.[84] They used atomic H, which is attained from the catalytically cracking of H_2 on the surface of the catalyst Pt, and the specific hydrogenation details are as follows: In order to showcase the efficacy of hydrogen spillover and mitigate the reaction conditions, a straightforward hydrogenation pathway was devised for crystalline TiO_2, involving the preloading of Pt onto TiO_2, followed by hydrogenation of the precursor, under H_2 atmospheric pressure and at a relatively low temperature. Figure 2-4 Route 2 shows a scheme of the noble metal-assisted H hydrogenation.

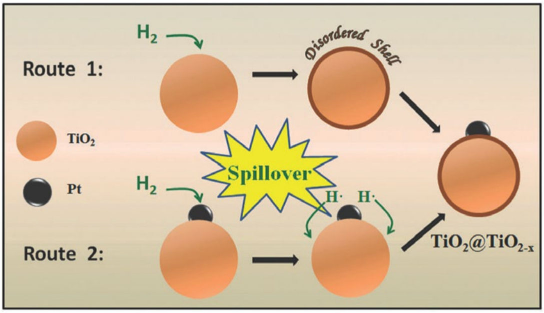

Fig. 2-4. Strategies for the hydrogenation of Pt promoted pristine TiO_2 to black TiO_2.

Based on the same working principle, Xu et al. in 2016 *Energy Environmental Science* reported the Pd-assisted hydrogenation of hydrogen atoms,[85] the details of which are shown in Figure 2-5.

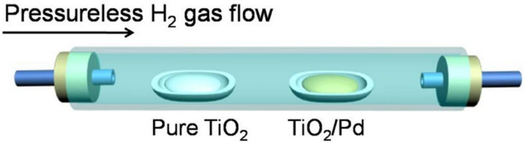

Fig. 2-5. Scheme of the facile hydrogenation of TiO_2 in the presence of Pd, in which ambient H_2/Ar (10%) gas flow is introduced.

To confirm the hypothesis of Pd-catalysed hydrogenation, rutile TiO_2 nanoparticles were synthesized with 0.43 mol% Pd loading (referred to as R/Pd) and subsequently subjected to treatment under a gas mixture of H_2/Ar (200 sccm and 10 vol% H_2). Remarkably, the colour of R/Pd rapidly transitioned from light yellow to black within a few seconds. Furthermore, upon exposure to open air while under the same H_2/Ar gas flow, the sample self-heated to temperatures exceeding 250°C in a prompt manner, in addition to the swift colour change to black.

Electrochemical reduction

In order to further develop new and efficient hydrogenation methods, Li et al. reported in 2014 *Mater. Chem.* the preparation of black TiO_2 by electrochemical reduction,[48] and the specific hydrogenation details are as follows: The anatase TiO_2 films were initially subjected to a short activation treatment (at 60 V for 30 s or 4 V for 600 s) in the anodization electrolyte described above. Subsequently, a cathodic voltage (e.g., -40 V for 200 s) was applied to electrochemically modify the sample in a 0.27 wt.% NH4F ethylene glycol solution. Figure 2-6 shows the preparation steps of black TiO_2 nanotubes by electrochemical reduction and the colour changes at different stages.

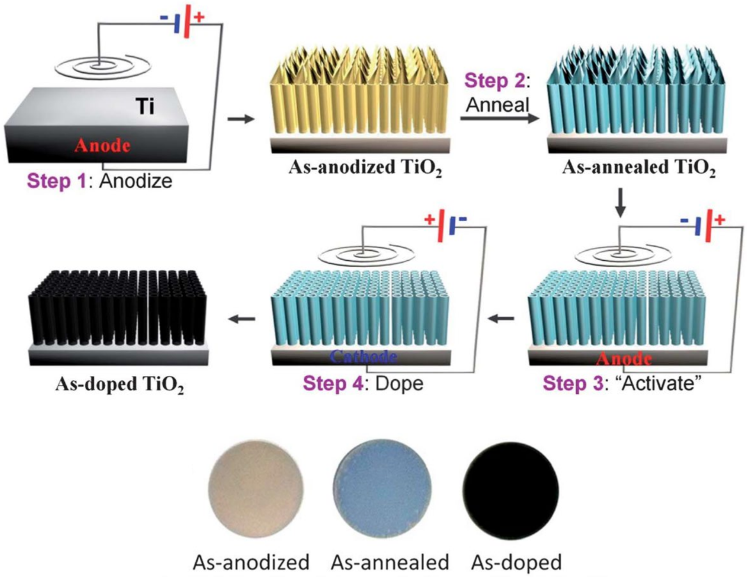

Fig. 2-6. Scheme of black TiO_2 nanotubes by electrochemical reduction and the corresponding colour changes.

It is worth noting that the doping technique described in this study facilitates the development of innovative, energy-efficient, electrochromic systems capable of maintaining their colour state for extended periods without the need for electrical power consumption. Additionally, this method has the potential to be applied to enhance the properties of other anodic metal oxides. Nevertheless, due to its nature as a chemical reduction process, the presence of chemical residues following hydrogenation is inevitable, rendering it an imperfectly clean method of hydrogenation.

High-energy proton implantation

Liu et al. reported in 2015 *Nano Lett.* a new method for the preparation of black TiO_2 nanotubes by high-energy proton implantation,[64] and the specific hydrogenation details are as follows: TiO_2 nanotube arrays of different lengths (1-12 μm) were utilized in this study, which were fabricated through self-organizing anodization and subsequently annealed to anatase. The samples were then subjected to proton (p^+) ion implantation at an energy of 30 keV and a dose of 10^{16} ions cm^{-2} using a Varian 350 D ion implanter. Figure 2-7 illustrates the steps for the preparation of black TiO_2 by this method.

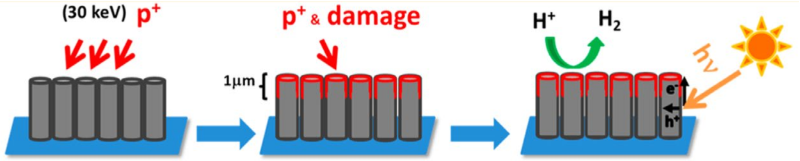

Fig. 2-7. Scheme of black TiO_2 prepared by high-energy proton implantation.

Ionic liquid gating

Lu et al. invented in 2017 *Nature* a new method: Ionic liquid gating (ILG) to prepare hydrogenated $SrCoO_{2.5}$ material,[86] the details are as follows: Prior to the ILG process, the edges of the thin films were coated with a gold electrode using direct-current ion sputtering or painted with a silver conductive adhesive to serve as the bottom electrode. Following this, platinum wires were attached to the bottom electrode through the application of indium pressure or silver conductive adhesive, while a platinum wire was utilized as the gate electrode. Subsequently, a minute quantity of ionic liquid was introduced to envelop the entirety of the film surface and the affixed platinum wire. The voltage between the lower electrode and the gate electrode was initially established at 0 V and gradually increased to the specified level within approximately one minute. This gating voltage was subsequently sustained until the phase transitions had concluded. Figure 2-8 shows a schematic diagram of the device for the